

Water Budget and Precipitation Efficiency of Typhoon Morakot (2009)

HSIAO-LING HUANG AND MING-JEN YANG

Department of Atmospheric Sciences, National Central University, Chung-Li, Taiwan

CHUNG-HSIUNG SUI

Department of Atmospheric Sciences, National Taiwan University, Taipei, Taiwan

(Manuscript received 13 February 2013, in final form 22 August 2013)

ABSTRACT

In this study, the Weather Research and Forecasting model, version 3.2, with the finest grid size of 1 km is used to explicitly simulate Typhoon Morakot (2009), which dumped rainfall of more than 2600 mm in 3 days on Taiwan. The model reasonably reproduced the track, the organization, the sizes of the eye and eyewall, and the characteristics of major convective cells in outer rainbands. The horizontal rainfall distribution and local rainfall maximum in the southwestern portion of the Central Mountain Range (CMR) are captured. The simulated rain rate and precipitation efficiency (PE) over the CMR are highly correlated. In the absence of terrain forcing, the simulated TC's track is farther north and rainfall distribution is mainly determined by rainbands. The calculated rain rate and PE over the CMR during landfall are about 50% and 15%–20% less than those of the full-terrain control run, respectively. By following major convective cells that propagate eastward from the Taiwan Strait to the CMR, it is found that the PE and the processes of vapor condensation and raindrop evaporation are strongly influenced by orographic lifting; the PEs are 60%–75% over ocean and more than 95% over the CMR, respectively. The secondary increase of PE results from the increase of ice-phase deposition ratio when the liquid-phase condensation becomes small as the air on the lee side subsides and moves downstream. This nearly perfect PE over the CMR causes tremendous rainfall in southwestern Taiwan, triggering enormous landslides and severe flooding.

1. Introduction

The steep terrain of the Central Mountain Region (CMR) in Taiwan can deflect tropical cyclones' (TCs') track, modify TCs' structures and rainfall distributions, and enhance TCs' rainfall amounts (Yeh and Elsberry 1993a,b; Wu and Kuo 1999; Wu et al. 2002; Lin et al. 2005; Lee et al. 2008; Jian and Wu 2008; Yang et al. 2008, 2011b). In addition, the steep terrain of Taiwan's CMR can also significantly modify TCs' water budgets and precipitation efficiencies as TCs encounter the CMR (Sui et al. 2007; Yang et al. 2011a).

Malkus and Riehl (1960) indicated that vapor evaporation from the ocean surface was essential for the TC development and maintenance. Kurihara (1975) found that the total (horizontal and vertical) vapor advection

mainly balanced with net condensation in his budget calculation of a simulated axisymmetric TC. Using the radar and aircraft observation data of Hurricane Allen (1980), Marks and Houze (1987) pointed out the dominance of the local (in situ) production of water by condensation process in the stratiform region within the radar volume. Based on the diagnostics of the 2-km model output of Hurricane Bonnie (1998), Braun (2006) showed that cloud condensate was precipitated out as fast as it was produced, and snow particles ejected outward from the eyewall grew further by deposition and aggregation processes in outer rainbands and fell out eventually as stratiform rainfall.

Precipitation efficiency (PE) is an important physical quantity in vapor, cloud, and surface rainfall budgets. The PE has been studied for more than 50 years (Braham 1952), and it has been applied to determine the rainfall intensity of the flash flood in operational precipitation forecasts (Doswell et al. 1996) and various precipitation process studies (Auer and Marwitz 1968; Heymsfield and Schotz 1985). There are several ways to

Corresponding author address: Dr. Ming-Jen Yang, Department of Atmospheric Sciences, National Central University, 300 Chung-Da Road, Chung-Li, 320, Taiwan.
E-mail: mingjen@cc.ncu.edu.tw

define and calculate the PE (Doswell et al. 1996; Ferrier et al. 1996; Li et al. 2002a,b; Sui et al. 2005, 2007). The cloud microphysics precipitation efficiency (CMPE) is defined as the ratio of total precipitation with respect to total condensation (liquid and ice phases). The CMPE is equivalent to the large-scale precipitation efficiency (LSPE), defined as the ratio of total precipitation to the large-scale vapor convergence, after taking average over a large area and a long period of time (Sui et al. 2005, 2007).

Yang et al. (2008) conducted a numerical simulation for Typhoon Nari (2001) with the finest grid size of 2 km and found that Nari's accumulated rainfall on Taiwan was linearly proportional to the terrain height. Yang et al. (2011b) examined the structure changes and terrain-induced storm asymmetries after Nari's landfall on Taiwan by conducting a series of terrain-sensitivity experiments. Yang et al. (2011a) further investigated budgets for vapor, cloud, and precipitation of Nari, and indicated that precipitation efficiency was increased by 10%–20% over the outer-rainband region after landfall, resulting in enhanced surface rainfall over the Taiwan terrain.

Typhoon Morakot (2009) formed in the western North Pacific on 3 August 2009 and made landfall over Taiwan on 7 August 2009, producing the worst flooding over southern Taiwan in the past 50 years. Ge et al. (2010) and Hong et al. (2010) suggested that the record-breaking rainfall associated with Morakot resulted from the interaction between the typhoon itself and background monsoon circulation. In addition to the CMR topographic lifting effect, Ge et al. (2010), Lin et al. (2011), and Tao et al. (2011) emphasized the abundant moisture supply from the southwesterly flow for this unprecedented rainfall event. In fact, the extreme rainfall (>2600 mm) during 72 h (7–9 August) was accompanied by Morakot's highly asymmetric structure and the slow movement after landfall in Taiwan (Chien and Kuo 2011). Fang et al. (2011) and Huang et al. (2011) further indicated that if there were no Taiwan terrain, the Morakot's rainfall amount at southern Taiwan would be reduced by more than 50%, compared to the full-terrain control experiment.

Following the work of Yang et al. (2011a) for Typhoon Nari, this study will extend the investigation of water budget and PE to Typhoon Morakot (2009). Morakot and Nari are among the top five storms that produced the most 24-h accumulated rainfall on Taiwan in the past 50 years. Typhoons Nari (2001) and Morakot (2009) certainly have different characteristics of rainfall pattern, the track relative to Taiwan topography, and the synoptic-scale setting. If similar physical mechanisms contributing to the heavy orographic rainfall by

vapor and water budget calculations can be found for the two distinct storms, results from the water budget and PE analyses might be general enough to be applied to other landfalling TCs on Taiwan as well.

The objective of this study is to use the high-resolution model output to calculate the water budgets (vapor, cloud, and precipitation) and the PE of Typhoon Morakot to investigate the essential physical processes responsible for the heavy rainfall in southwestern Taiwan. In particular, by comparing with the simulated tracks, structures, precipitation patterns, rain rates, and the PEs of the full-terrain (CTL) and no-terrain (FLAT) simulations of Typhoon Morakot, we will examine the physical mechanisms responsible for the local torrential rainfall and high PE above the steep CMR on Taiwan.

2. Model description and initialization

The Advanced Research Weather Research and Forecasting model (ARW), version 3.2 (Skamarock et al. 2008), is used in this study to simulate the Morakot case. A total of three domains with horizontal grid sizes of 9, 3, and 1 km are used with 31 eta (η) levels in the vertical and a model top at 50 hPa (Fig. 1 and Table 1). Two-way feedbacks are allowed between all domains. The physical schemes used in the full-terrain control simulation (CTL) include the Weather Research and Forecasting model (WRF) single-moment 6-class microphysics scheme (WSM6; Hong and Lim 2006), Yonsei University (YSU) planetary boundary layer (PBL) parameterization (Hong and Pan 1996; Hong et al. 2006), and Dudhia (1989) shortwave and Rapid Radiative Transfer Model (RRTM) longwave (Mlawer et al. 1997) schemes. Note that no cumulus parameterization scheme is used in all three domains. The initial and boundary conditions are from the European Centre for Medium-Range Weather Forecasts (ECMWF)/Tropical Ocean Global Atmosphere (TOGA) datasets with 6-hourly gridded analyses at 1.125° latitude–longitude resolution. The integration starts from 0000 UTC 6 August 2009, with a forecast length of 96 h.

The no-terrain sensitivity experiment is conducted, in which all model parameters are held the same as those in the CTL simulation, except that 1-m flat terrain elevation on Taiwan (FLAT) is used. The 31 η levels are located at 1.00, 0.99, 0.98, 0.96, 0.94, 0.92, 0.90, 0.87, 0.84, 0.81, 0.78, 0.75, 0.72, 0.69, 0.65, 0.61, 0.57, 0.53, 0.49, 0.45, 0.41, 0.37, 0.33, 0.29, 0.25, 0.21, 0.17, 0.13, 0.09, 0.05, and 0.

3. Model verification and results

In this section, we will show the simulated track, strength, and the structure of eye, eyewall, spiral rainband,

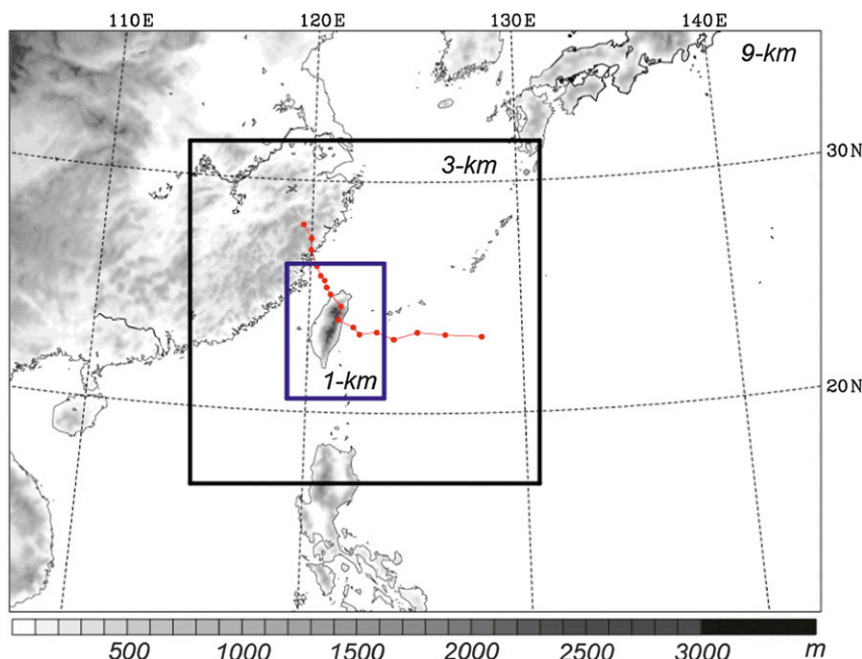


FIG. 1. The triply nested WRF domains (at horizontal grid size of 9, 3, and 1 km, respectively) and the topography (m, gray shading; scale at bottom), superimposed on the 6-hourly best track (red) of Typhoon Morakot from 0000 UTC 6 Aug to 0000 UTC 10 Aug 2009) issued by the CWB.

and precipitation distribution of Morakot in the CTL simulation, which are in reasonable agreement with the observations.

a. Track and horizontal storm structure

Figure 2a compares Morakot's tracks from the Central Weather Bureau (CWB) best-track analysis (OBS) and the model simulations (CTL and FLAT) on the 3-km domain, and Fig. 2b shows the corresponding storm intensities. In general, the CTL simulates Morakot's track very well, especially for its landfall position at Hualien, albeit 8–10 h later than and 17 km to the north of the observation. In the absence of Taiwan topography, the FLAT track is farther north than the OBS and CTL tracks after landfall (Fig. 2a). The CTL storm moved slowly to northwestern Taiwan during the landfall period, similar to the best-track analysis (OBS). The simulated storm is stronger than the observed, and the storm becomes stronger without the Taiwan terrain (Fig. 2b).

The horizontal radar reflectivity fields of the OBS, CTL, and FLAT experiments (on a 3-km grid) at 1100 and 1200 UTC August 2009 are shown in Fig. 3. The CTL reproduces well the structure and local intensification of Morakot's outer rainbands in southwestern Taiwan. These outer rainbands are enhanced by the interaction between the southwesterly monsoonal flow

from the Taiwan Strait and topographic lifting above mountains, producing heavy rainfall over the CMR. The horizontal scales of Morakot's west–east-oriented rainbands and south–north-oriented rainfall maxima (>45 dBZ) over the CMR are about 180–200 and 50–60 km, respectively. The combined pattern of these two rainfall features appears as a “T” shape (Figs. 3a–d). Without the terrain forcing, the west–east-oriented rainbands are the dominant rainfall features in the FLAT experiment and their along-line horizontal scales are more than 300 km (Figs. 3e–f).

b. Accumulated rainfall

Figure 4 shows the 24- (Figs. 4a–c) and 72-h (Figs. 4d–f) accumulated rainfalls over Taiwan. The observed torrential rainfall reached 2683 mm during 72 h (0000 UTC 7 August–0000 UTC 10 August) in central and southern

TABLE 1. The model design.

Domain	D1	D2	D3
Dimensions (x, y)	416 × 301	541 × 535	451 × 628
Grid size (km)	9	3	1
Area coverage ($\text{km} \times \text{km}$)	3735 × 2700	1620 × 1602	450 × 627
Time step (s)	30	10	3.33
Integration duration (h)	0–96	0–96	0–96

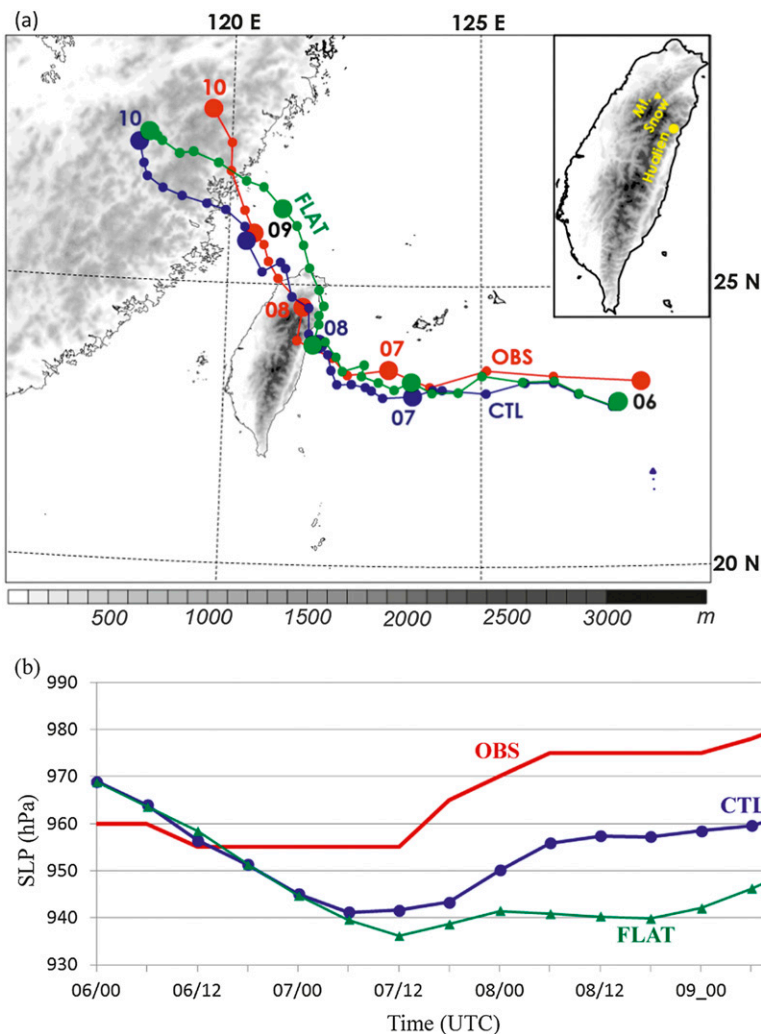


FIG. 2. (a) Comparison of the best track (OBS; red, every 6 h) and the simulated tracks (CTL in blue and FLAT in green, every 3 h) of Typhoon Morakot, superimposed on the terrain height (gray shading). Each big dot denotes Morakot's center position every 24 h. Inset is for detailed Taiwan terrain and locations of Mount Snow and Hualien. (b) Time series of the minimum sea level pressure (SLP; hPa) of the best-track analysis (OBS; red) and the simulated storms (CTL in blue and FLAT in green) of Typhoon Morakot.

Taiwan (Fig. 4d). The heavy rainfall was associated with the enhancement of the typhoon's west-east rainbands by the orographic lifting. The simulated 72-h rainfall maximum in the CTL is overestimated in central Taiwan (3392 mm; see Fig. 4e), probably because of the insufficient rain gauge stations in the CMR, the accumulation of model errors, and the deficiency of the single-moment microphysical parameterization scheme. Because the CTL track is slightly to the south of the OBS track (Fig. 2), this track error results in the fact that 24-h (0000 UTC 8 August–0000 UTC 9 August) rainfall amounts are underestimated at Chiayi and Tainan but overestimated at Kaohsiung and the CMR (Figs. 4a,b).

To examine the temporal evolution of the typhoon-induced rainfall in southwestern Taiwan, we choose a rectangular box region over the CMR (22.72°–23.72°N, 120.53°–121.03°E; see Fig. 5a). The box-averaged rain rates calculated with the rain gauge data (OBS) and 1-km model results (from the CTL and FLAT) are shown in Fig. 5b. It is clear in Fig. 5b that the time series of CTL rain rate matched the observed time series very well, especially during Morakot's landfall period (0000 UTC 8 August–0000 UTC 9 August). In particular, the maximum CTL rain rate averaged over the box area ($\sim 50 \text{ mm h}^{-1}$) is slightly higher than the OBS ($\sim 47 \text{ mm h}^{-1}$). In the absence of CMR terrain lifting, the peaked FLAT rain

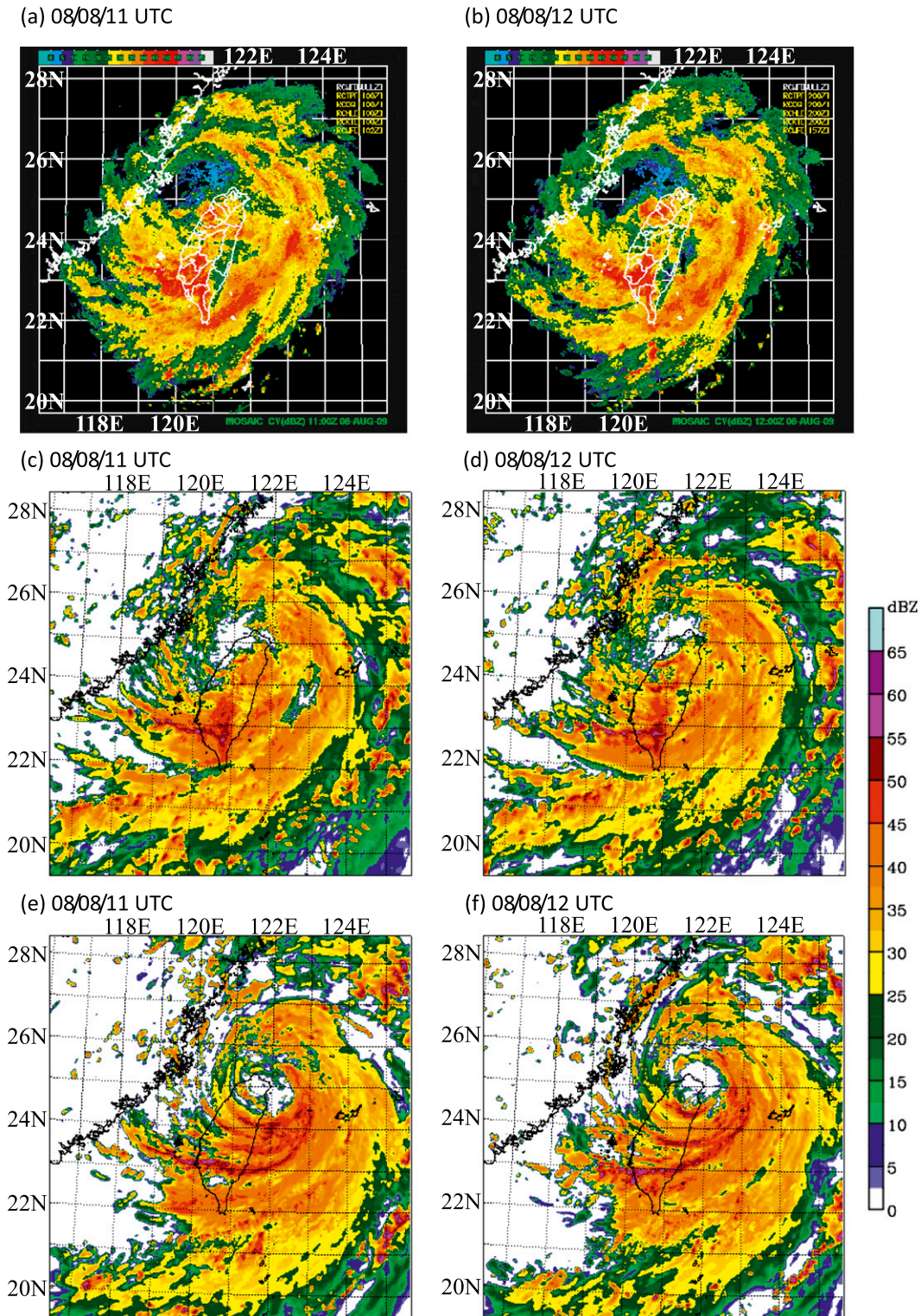


FIG. 3. Horizontal distribution of vertical-column maximum (CV) radar reflectivity (dBZ) at 1100 UTC 8 Aug 2009 for the (a) OBS, (c) CTL, and (e) FLAT runs and at 1200 UTC 8 Aug 2009 for the (b) OBS, (d) CTL, and (f) FLAT runs. The radar reflectivity CVs of (c)–(f) are from the 3-km grid.

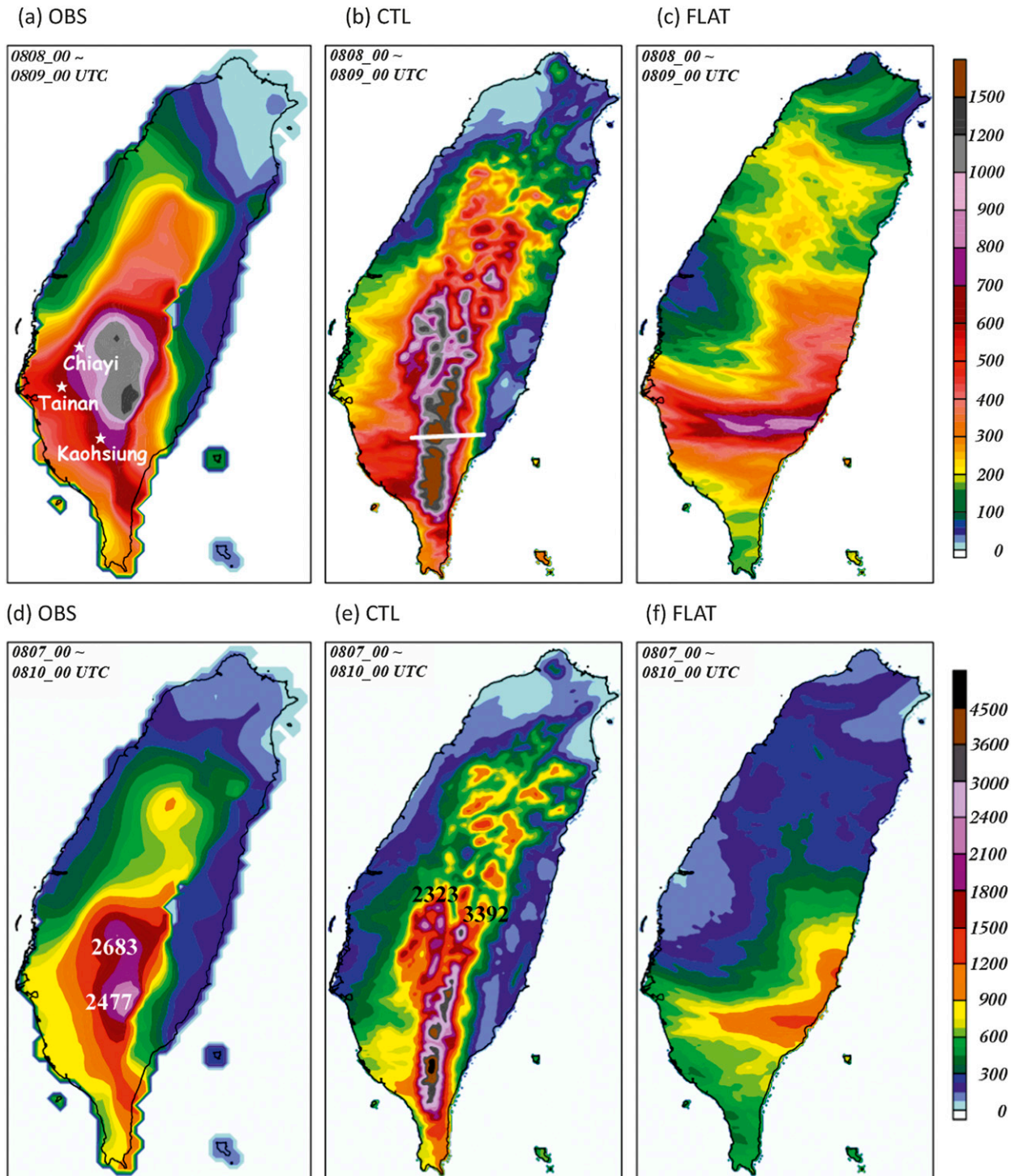


FIG. 4. Horizontal maps of the 24-h accumulated rainfall (mm) of the (a) OBS, (b) CTL, and (c) FLAT runs from 8 to 9 Aug, and of the 72-h accumulated rainfall (mm) of the (d) OBS, (e) CTL, and (f) FLAT runs from 7 to 10 Aug on Taiwan. All time periods begin and end at 0000 UTC, and the rainfall amounts of (b),(c),(e), and (f) are from the 1-km grid. Locations of Chiayi, Tainan, and Kaohsiung are indicated in (a) and the horizontal position for the vertical cross section in Fig. 13 is shown in (b).

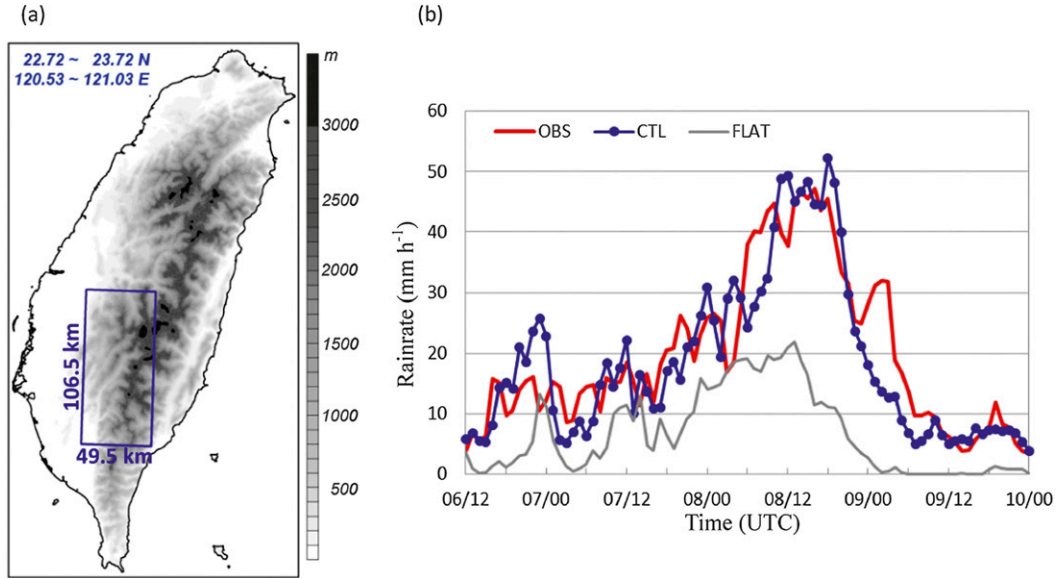


FIG. 5. (a) Horizontal maps of terrain height over Taiwan (gray shading), and (b) time series of rain rates for the OBS (red), CTL (blue), and FLAT (gray) runs from 1200 UTC 6 Aug to 0000 UTC 10 Aug 2009 on the 1-km grid. Blue box in (a) is the area for the time series in (b) and for water budget calculations in Fig. 8.

rate averaged over the box area ($17\text{--}22\text{ mm h}^{-1}$) is only 30%–40% of the OBS and CTL, indicating the dominance of terrain forcing for the rainfall maximum in southwestern Taiwan (Fang et al. 2011; Huang et al. 2011).

c. Water budget and precipitation efficiency

Following the water budget formulation of Braun (2006) and Yang et al. (2011a), we calculate the vapor, cloud, and precipitation budgets within the TC vortex of Morakot prior to and after its landfall on Taiwan, and for major convective cells along the west–east rainbands across the CMR. The governing equation for water vapor q_v in an Eulerian framework can be written as

$$\frac{\partial q_v}{\partial t} = \frac{1}{\mu} \left[-\nabla \cdot (q_v \mathbf{V}) - \frac{\partial(q_v W)}{\partial z} + q_v \left(\nabla \cdot \mathbf{V} + \frac{\partial W}{\partial z} \right) + D_v \right] - C + E + B_v + \text{Resd}_v, \quad (1)$$

Similarly, the equation for cloud ($q_c = q_l + q_i$) can be written as

$$\frac{\partial q_c}{\partial t} = \frac{1}{\mu} \left[-\nabla \cdot (q_c \mathbf{V}) - \frac{\partial(q_c W)}{\partial z} + q_c \left(\nabla \cdot \mathbf{V} + \frac{\partial W}{\partial z} \right) + D_c \right] + Q_{c+} - Q_{c-} + B_c + \text{Resd}_c, \quad (2)$$

and the equation for precipitation ($q_p = q_r + q_s + q_g$) can be written as

$$\frac{\partial q_p}{\partial t} = \frac{1}{\mu} \left[-\nabla \cdot (q_p \mathbf{V}) - \frac{\partial(q_p W)}{\partial z} + q_p \left(\nabla \cdot \mathbf{V} + \frac{\partial W}{\partial z} \right) + D_p \right] + \frac{\partial(q_p V_T)}{\partial z} + Q_{p+} - Q_{p-} + \text{Resd}_p, \quad (3)$$

where q_v , q_c , and q_p are the water vapor, cloud [cloud water (q_l) and cloud ice (q_i)], and precipitation [rainwater

TABLE 2. Water budget parameter description.

Name	Description
Cond _T	Total condensation and deposition
Cond _C	Cloud water condensation
Dep _S	Snow deposition
Dep _G	Graupel deposition
Dep _I	Cloud ice deposition
Evap _R	Evaporation of raindrop
Evap _S	Evaporation of melting snow
Evap _G	Evaporation of melting graupel
Mlt _S	Snow melting
Mlt _G	Graupel melting
Evap	Total evaporation and sublimation
HFP	Inward-directed (positive) horizontal flux convergence
HFN	Outward-directed (negative) horizontal flux convergence
HFC	HFP + HFN (net horizontal flux convergence)
VFC	Vertical flux convergence
Div	Divergence term
P	Precipitation flux
Diff	Numerical diffusion
PBL	Boundary layer source and vertical (turbulent) diffusion
Tend	Storage term
Resd	Residual term

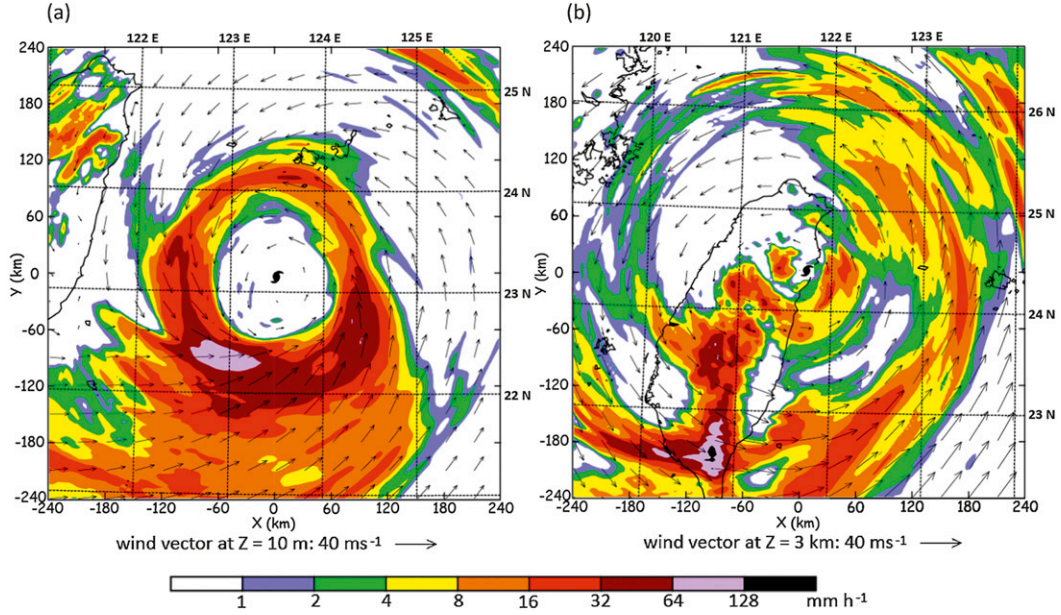


FIG. 6. Horizontal distribution of the 1-h accumulated rainfall (mm) and 1-h-averaged horizontal wind vector of the CTL run (a) from 0000 to 0100 UTC 7 Aug and (b) from 0730 to 0830 UTC 8 Aug 2009. The horizontal winds are at $z = 10$ m in (a) and at $z = 3$ km in (b), and the typhoon center is indicated with the black typhoon symbol.

(q_r), snow (q_s), and graupel (q_g)] mixing ratios; \mathbf{V} (U, V) and W are the pressure-weighted horizontal wind vector and vertical velocity, and they are defined as $U = \mu u$, $V = \mu v$, and $W = \mu w$; $\mu = \pi_s - \pi_t$, μ is the vertical-column mass defined as the difference between surface (π_s) and model top (π_t) pressures; V_T is the hydrometeor terminal velocity; Q_{c+} , Q_{c-} , Q_{p+} , and Q_{p-} are the cloud and precipitation microphysical source (plus sign) and sink (minus sign) terms; C is the condensation and deposition; E is the evaporation and sublimation; $C - E = Q_{c+} - Q_{c-} + Q_{p+} - Q_{p-}$; B_v and B_c are the contributions from the planetary boundary layer parameterization and vertical turbulent diffusion to the vapor and cloud budgets; and D_v , D_c , and D_p are numerical diffusion terms for vapor, cloud, and precipitation, respectively. Each water budget term in Eqs. (1)–(3) is volumetrically integrated either within Morakot’s vortex circulation ($r < 240$ km) or for a rectangular box area over the CMR; then, the results are averaged temporally for an hour with a data interval of 2 min. All budget terms are normalized by the total condensation and deposition C . Using the shorthand notations in Table 2, the water vapor budget described in Eq. (1) can be written as

$$\begin{aligned} \text{Tend} = & \text{HFC} + \text{VFC} + \text{Div} + \text{Diff} + \text{Cond}_T \\ & + \text{Evap} + \text{PBL} + \text{Resd} \end{aligned} \quad (4)$$

Similarly, the water condensate (cloud and precipitation) budget determined by combining Eqs. (2) and (3) can be written as

$$\begin{aligned} \text{Tend} = & \text{HFC} + \text{VFC} + \text{Div} + \text{Diff} + P - \text{Cond}_T \\ & - \text{Evap} + \text{PBL} + \text{Resd} \end{aligned} \quad (5)$$

Cond_T is the total condensation and deposition, and by following Sui et al. (2007) for the revised definition of cloud microphysics PE (or CMPE2) it can be decomposed into several terms as

$$\text{Cond}_T = \text{SI}_{q_v} + \text{sgn}(Q_{\text{CM}})Q_{\text{CM}}, \quad (6a)$$

where $\text{sgn}(F) = 1$, when $F > 0$; $\text{sgn}(F) = 0$, when $F \leq 0$; and

$$Q_{\text{CM}} = \text{HFC} - P + \text{SI}_{q_v} - \text{SO}_{q_v}, \quad (6b)$$

$$\text{SI}_{q_v} = \text{Cond}_C + \text{Dep}_S + \text{Dep}_G + \text{Dep}_I, \quad \text{and} \quad (6c)$$

$$\text{SO}_{q_v} = \text{Evap}_R + \text{Evap}_S + \text{Evap}_G + \text{Mlt}_S + \text{Mlt}_G, \quad (6d)$$

where Q_{CM} is the sum of local hydrometeor change and hydrometeor convergence, HFC is the net horizontal flux convergence of q_c and q_p , and SI_{q_v} and SO_{q_v} are the sink and source terms of water vapor, respectively; the

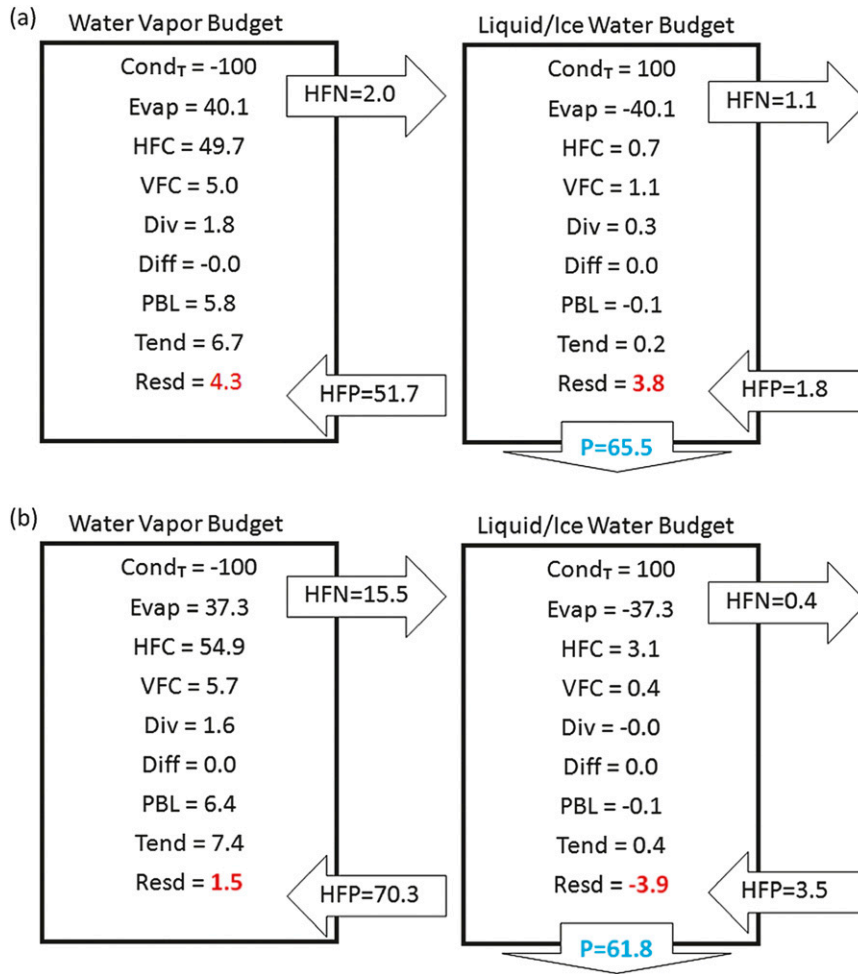


FIG. 7. Water vapor and liquid/ice water (cloud plus precipitation) budgets of Morakot (a) over ocean from 0000 to 0100 UTC 7 Aug and (b) after landfall from 0730 to 0830 UTC 8 Aug 2009. The time-averaged, volumetrically integrated budget terms are calculated within the vortex circulation ($r < 240$ km) from the 3-km grid (with a 2-min data interval) of the CTL run. Parameter names are provided in Table 2. All values are normalized by a Cond_T value of 100 within the radius of 240 km. Cond_T is $2.28 \times 10^{12} \text{ kg h}^{-1}$ over ocean in (a) and $1.67 \times 10^{12} \text{ kg h}^{-1}$ after landfall in (b).

definitions of each source and sink term are given in Table 2.

In addition, we use the water budget calculations to compute the precipitation efficiency as defined in Sui et al. (2005, 2007). Thus, the precipitation efficiency from the revised cloud microphysics perspective (CMPE2) is defined as

$$\text{PE} = P/\text{Cond}_T = P/[\text{SI}_{q_v} + \text{sgn}(Q_{CM})Q_{CM}], \quad (7)$$

where P is the time-averaged and volumetrically integrated amount of total precipitation flux, and it can be written as

$$P = \frac{\overline{\overline{\partial(q_p V_T)}}}{\partial z}, \quad (8)$$

where the double overhead bar indicates the temporal and volumetric average defined in Eq. (6) in Yang et al. (2011a).

Because Typhoon Morakot (2009) is a large TC with broad vortex circulation, a radius of 240 km (Fig. 6) is used to compute the volume-integrated water budget terms. Note that a radius of 150 km was used for volume-integrated budget terms of Typhoon Nari (2001) with a small vortex circulation [see Figs. 1 and 4 of Yang et al. (2011a)]. Figure 6 shows the 1-h accumulated rainfall and hourly averaged horizontal winds at $z = 10$ m while

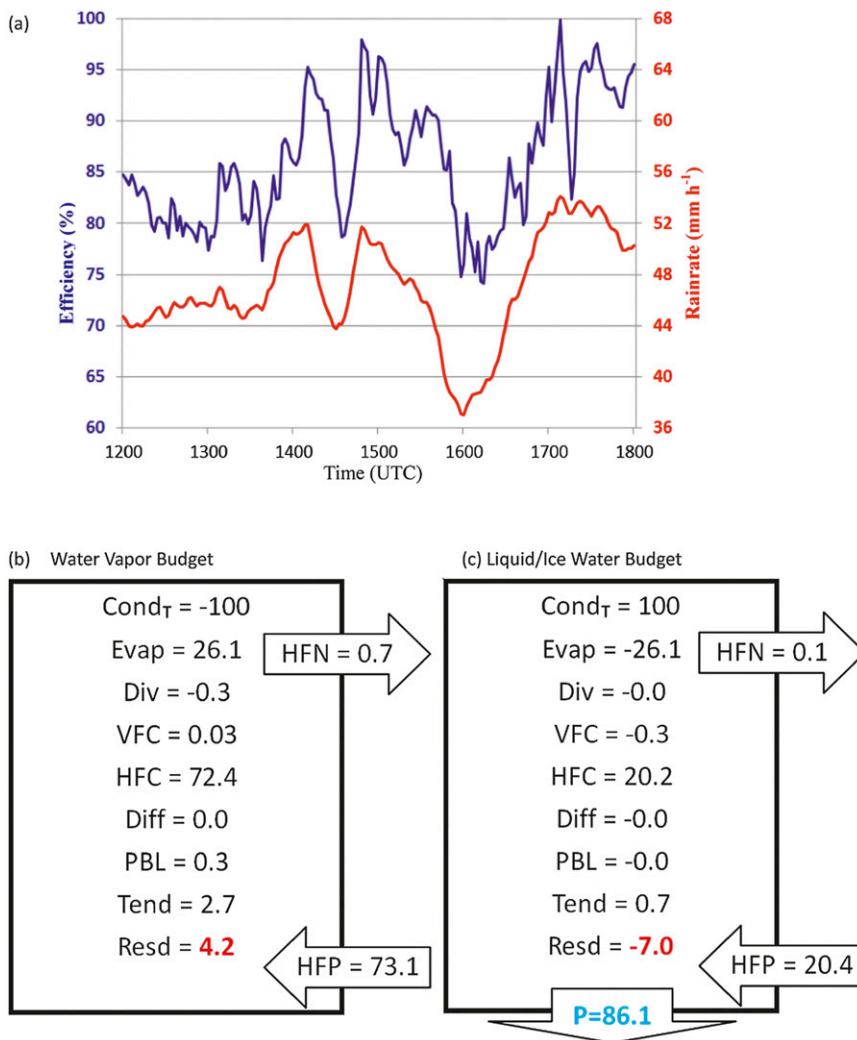


FIG. 8. (a) Time series of precipitation efficiency (blue) and rain rate (red) and (b) the time-averaged, volumetrically integrated water vapor budget, and (c) liquid/ice water (cloud plus precipitation) budgets of the CTL run from 1200 to 1800 UTC 8 Aug 2009. All are calculated from the 1-km grid (with a 2-min data interval) for the blue box in Fig. 5a. The efficiency (%; blue curve) corresponds to the left ordinate, and the rain rate (mm h⁻¹; red curve) corresponds to the right ordinate in (a).

Morakot was over ocean (0000–0100 UTC 7 August) and at $z = 3$ km while Morakot made landfall on Taiwan (0730–0830 UTC 7 August), respectively. For the oceanic Morakot, the vortex circulation structure is similar to that of Nari but with a more asymmetric and larger surface precipitation area [see Fig. 1 in Yang et al. (2011a)]. After landfall, the eastern half of the vortex circulation of Morakot is more organized than the western half. The inner core circulation ($r < 60$ km) is highly asymmetric with less rainfall (<45 dBZ or <32 mm h⁻¹) on the lee side of Mount Snow (northwestern Taiwan), owing to the blockage of the CMR. For the outer rainbands, surface rainfall rates are

stronger because of the combined effects of the southwesterly monsoon flow and the CMR orographic lifting.

Figure 7 shows the 1-h-averaged vapor and water budgets calculated within the vortex circulation (with a 240-km radius) of Morakot prior to and after landfall on Taiwan, based on the 3-km grid of the CTL run (with 2-min data interval). The change of water vapor budget of Typhoon Morakot during the landfall process is similar to that of Typhoon Nari, especially for the enhancement of low-level horizontal vapor flux (HFP) after landfall (70.3% versus 51.7% for Morakot; 112.8% versus 54.8% for Nari). While over the ocean, Morakot with a larger storm radius (240 km for Morakot versus

150 km for Nari) has more storm-total condensation than Nari ($2.28 \times 10^{12} \text{ kg h}^{-1}$ for Morakot, but $7.41 \times 10^{11} \text{ kg h}^{-1}$ for Nari). The PEs within Morakot vortex circulation ($r < 240 \text{ km}$) are 65.5% and 61.8% at the oceanic and landfall stages, respectively. The net inward horizontal water vapor flux convergence (HFC) after landfall is stronger than that over ocean (54.9% versus 49.7% for Morakot and 80.6% versus 46.9% for Nari), producing stronger rainfall rate after landfall (peak rainfall rate of greater than 128 mm h^{-1} over land versus $64\text{--}128 \text{ mm h}^{-1}$ over ocean; Figs. 6a,b). Note that unlike the case of Nari, the storm-total condensation and deposition of Morakot is reduced from $2.28 \times 10^{12} \text{ kg h}^{-1}$ over the ocean to $1.67 \times 10^{12} \text{ kg h}^{-1}$ after landfall, owing to the enhanced evaporation and sublimation of a larger precipitation-void inner core of Morakot (Fig. 6b). Note that after landfall on Taiwan, both Morakot and Nari have enhanced water vapor convergence, increased PE, and greater surface landfall, despite their different track and storm structure.

Figure 8a shows the time series of the calculated PE [the CMPE2 using Eq. (7)] and surface rainfall rate over the box area above the CMR. They are computed from the 1-km grid output (with 2-min data interval) of the CTL run above the rectangular area over the CMR (the blue box in Fig. 5a) during 60–66 h (1200–1800 UTC 8 August 2009). Results indicate that the PE is highly correlated with the surface rain rate; in particular, the PE is greater than 75% during the 6-h period, and it can even reach to more than 95% at some instants (Fig. 8a). Note that around 1600 UTC, the PEs remain relatively high (75%–80%) but the rain rates drop significantly (Fig. 8a). It is because the weaker convective cells (with less rainwater at low levels but more cloud ice and snow at upper levels) from the Taiwan Strait produced a decreasing surface rain rate but with a high PE (less condensation to liquid drops but more deposition to ice crystals).

Figures 8b and 8c are the corresponding vapor and liquid/ice water budgets, which are calculated with Eqs. (4) and (5) [similar to Figs. 14 and 15 in Yang et al. (2011a)]. The net horizontal flux convergence of water vapor (HFC) is 72.4%, which is the dominant term in the water vapor budget and is associated with the persistent transport of abundant moisture from the ambient oceanic environment and continuous generation of convective cells along the quasi-stationary rainbands (Fig. 3). The water vapor flux divergence (HFN = 0.7%) averaged over the box area in a 6-h period is much smaller than that averaged within the large vortex circulation in a 1-h period (HFN = 15.5%; Fig. 7b), and they are less than that for Nari [HFN = 32.2%; see Fig. 14b of Yang et al. (2011a)], probably because of the

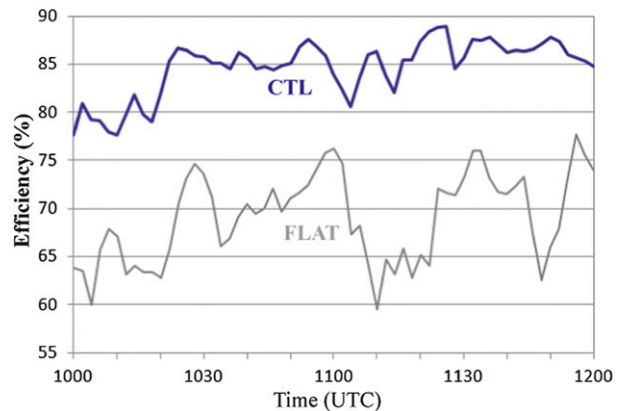


FIG. 9. Time series of precipitation efficiency for the CTL (blue) and FLAT (gray) runs calculated from the 1-km grid (with a 2-min data interval) for the blue box in Fig. 5a from 1000 to 1200 UTC 8 Aug 2009.

weaker upper-level radial outflow of Morakot. The high PE of 86.1%, averaged for 6 h, indicates that the water vapor transported inward along the west–east rainbands by the horizontal flux convergence quickly converts into cloud drops and ice crystals (HFP = 73.1% in Fig. 8b), and then produced raindrops, graupel, and snow particles being transported into the box area by the rainbands (HFP = 20.4% in Fig. 8c). According to above results, the PEs (>85%) for the box area above the CMR have a higher efficiency than those within the whole TC vortex structures [PE = 61.8% for Morakot (Fig. 7b) and 70% for Nari; see Fig. 16a of Yang et al. (2011a)]. This indicates that the orographic lifting by the CMR plays a more important role in generating heavier rainfall in a localized area that was frequently traversed by convective cells along the quasi-stationary west–east rainbands.

To examine the rainfall enhancement effect by orographic forcing, we also calculate the PE at the same box area in the FLAT run. Note that Figs. 3c and 3e compare the radar reflectivity fields between the CTL and FLAT runs at 1100 UTC 8 August; the CTL storm has strong echoes along outer rainbands and convective cells are phase locked to the CMR with a “T” shape, but the FLAT storm only shows strong echoes along outer rainbands. Figure 9 illustrates that during a 2-h period, the PE in the no-terrain (FLAT) run is only 59%–77%, which is significantly less than that of the full-terrain (CTL) run (78%–88%). It clearly demonstrates that the terrain lifting by the CMR increases the precipitation efficiency by 10%–20% during the 2 h.

d. Lagrangian framework discussion

To understand the microphysics evolution from a Lagrangian perspective, we follow four major convective

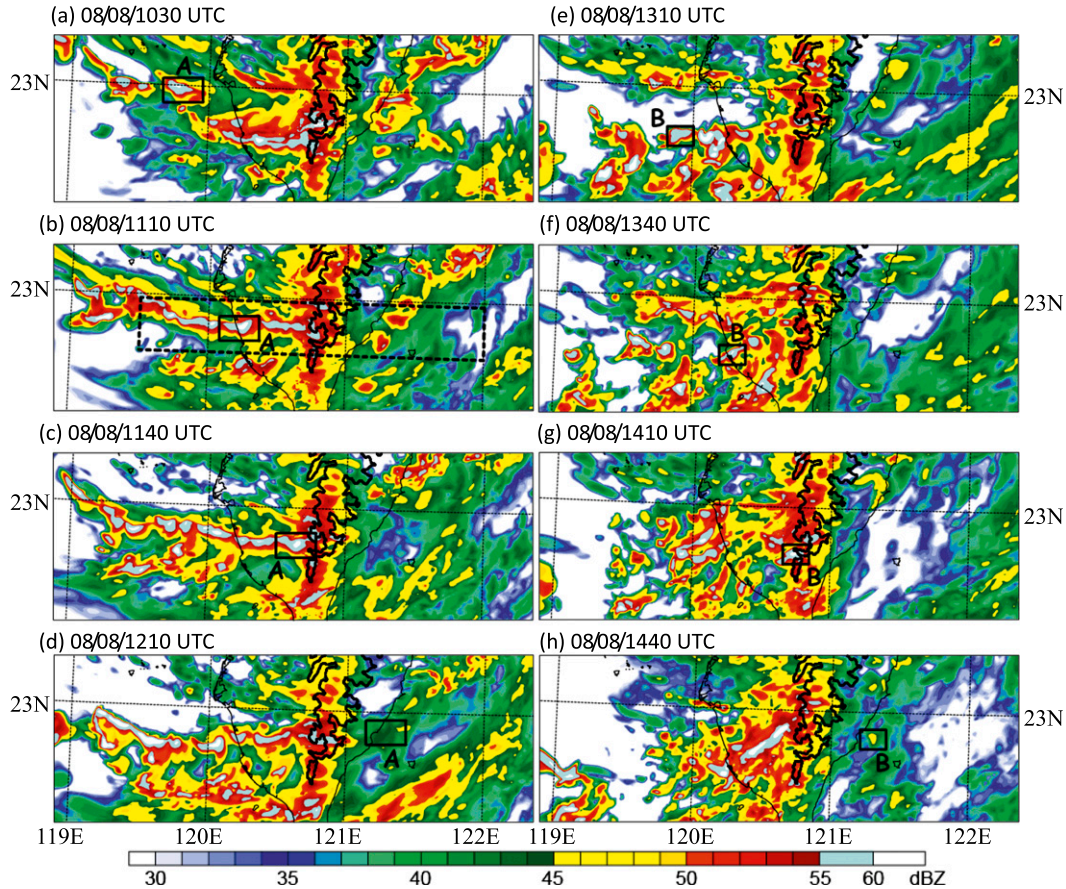


FIG. 10. Horizontal distribution of vertical-column maximum (CV) radar reflectivity (dBZ) for cell A at (a) 1030, (b) 1110, (c) 1140, and (d) 1210 UTC and for cell B at (e) 1310, (f) 1340, (g) 1410, and (h) 1440 UTC 8 Aug 2009 from the 1-km CTL run. The dimensions of the black boxes for cells A and B are $30 \text{ km} \times 20 \text{ km}$ and $20 \text{ km} \times 16 \text{ km}$, respectively. The solid line is the 1500-m terrain elevation. Rectangular dashed box in (b) is for the horizontal cross section shown in Fig. 15a.

cells that originally developed from the Taiwan Strait, moved eastward along the west–east rainbands and impinged on the CMR, and then dissipated on the lee side of CMR. High-resolution model output from the 1-km grid with a 2-min data interval is used in the calculation of microphysical budget terms in this subsection. The evolution of horizontal distribution of vertically maximum radar echoes of convective cells A and B within the rainbands are shown in Fig. 10, and similar evolution for convective cells C and D are shown in Fig. 11. The sizes of cells A and B are rectangle boxes of $30 \text{ km} \times 20 \text{ km}$ and $20 \text{ km} \times 16 \text{ km}$, respectively, and the sizes of cells C and D are both rectangle boxes of $24 \text{ km} \times 16 \text{ km}$. Two distinct rainfall regimes for four convective cells are further chosen: oceanic rainfall regime (1030–1110 UTC for cell A, 1310–1340 UTC for cell B, 0740–0810 UTC for cell C, and 0750–0820 UTC for cell D) and mountain rainfall regime (1110–1210 UTC for cell A, 1340–1440 UTC for cell B, 0810–0850 UTC for cell C, and 0820–0900 UTC for cell D).

To elaborate the difference of PEs between the oceanic and mountain rainfall regimes, we further divide the microphysics ratio into three different components. Three microphysics ratios as the condensation ratio (CR), deposition ratio (DR), and evaporation ratio (ER) are defined as

$$\text{CR} = \text{Cond}_C / \text{Cond}_T, \quad (9)$$

$$\text{DR} = (\text{Dep}_S + \text{Dep}_G + \text{Dep}_I) / \text{Cond}_T, \quad \text{and} \quad (10)$$

$$\text{ER} = \text{Evap}_R / \text{Cond}_T, \quad (11)$$

where the definitions of water budget terms in Eqs. (9)–(11) are given in Table 2. Figure 12 displays the cells' Lagrangian evolution of precipitation efficiency [CMPE2 as defined in Eq. (7)], condensation ratio [CR as defined in Eq. (9)], deposition ratio [DR as defined in Eq. (10)], evaporation ratio [ER as defined in Eq. (11)], and the averaged terrain height underneath cells A and B.

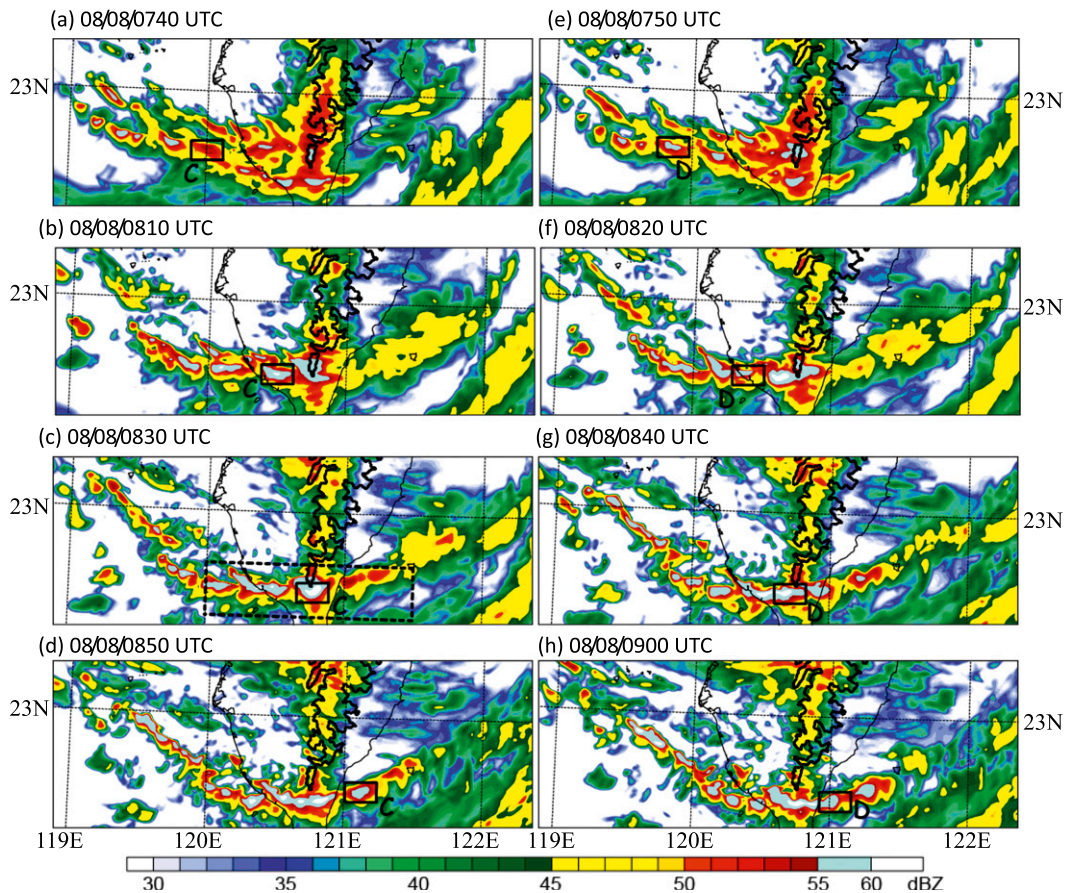


FIG. 11. As in Fig. 10, but for cell C at (a) 0740, (b) 0810, (c) 0830, and (d) 0850 UTC and for cell D at (e) 0750, (f) 0820, (g) 0840, and (h) 0900 UTC 8 Aug 2009 from the 1-km CTL run. The dimensions of black boxes for cells C and D are both $24 \text{ km} \times 16 \text{ km}$. The solid line is the 1500-m terrain elevation. Rectangular dashed box in (c) is for the horizontal cross section shown in Fig. 15b.

(Similar time series for the Lagrangian evolution of precipitation efficiency and three microphysics ratios for cells C and D are illustrated in Fig. 14). For cell A along the primary outer rainband, the PE is 60%–75% for the oceanic rainfall regime and 35%–100% for the mountain rainfall regime, respectively (Fig. 12a). On the other hand, for cell B along the secondary outer rainband, the PE is 43%–74% for the oceanic regime and 35%–100% for the mountain regime (Fig. 12b). The evolution of CR is qualitatively similar to that of PE, with an increasing trend on the windward slope and a decreasing trend on the lee side, indicating the dominance of liquid-phase microphysical process on Morakot-induced rainfall above the rugged terrain.

In contrast, the temporal variations of DR and ER are out of phase with those of PE and CR, as following the movement of cells A and B. For cell A, DR is 4%–9% over the ocean, 4%–8% on the windward slope, and 3%–26% on the lee side (Fig. 12a). Similar evolution of

DR is found for cell B but with a larger magnitude on the lee side ($\text{DR} > 40\%$). ER of raindrops are decreased on windward side (0%–4%) but significantly increased on the lee side (4%–30%) for both cells A and B. The large increase of raindrop evaporation results in the sharp decrease of PE on the lee side, and the gradual and gentle increase of liquid-phase condensation (CR) mainly leads to the increase of PE on the windward side.

The PEs are increased again farther downstream from the lee side (from 1204 to 1210 UTC in Fig. 12a for cell A, from 1434 to 1444 UTC in Fig. 12b for cell B, from 0850 to 0900 UTC in Fig. 14a for cell C, and from 0902 to 0916 UTC in Fig. 14b for cell D). The secondary increase of the PEs results from the increase of ice-phase DR, when the liquid-phase condensation becomes small as the air on the lee side subsides and moves downstream. Figure 13 shows clearly the orographic lifting and vertically propagating gravity waves above the terrain [also see Fig. 12 in Tang et al. (2012)], which is helpful to

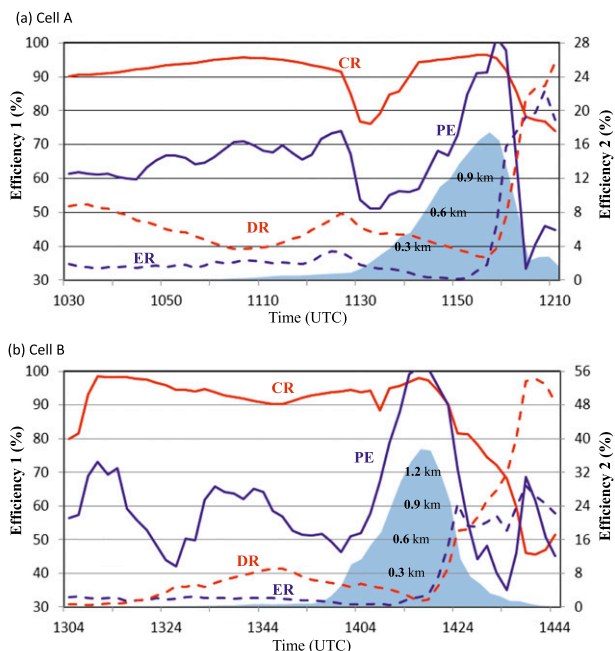


FIG. 12. Time series of PE, CR, DR, and ER for (a) cell A and (b) cell B calculated within the black boxes on the 1-km grid shown in Fig. 10. The light blue shading is terrain height passed by cells A and B. The PE (blue solid) and CR (red solid) correspond to efficiency 1 (left ordinate), and DR (red dashed) and ER (blue dashed) correspond to efficiency 2 (right ordinate).

transport hydrometeors upward and downstream to the lee side. Note that raindrop ER gradually reduces to zero as convective cells move upslope as a result of the near-saturated environmental moisture in the ascending process (Figs. 12a,b). A similar result is also found for a minimum of total evaporation near the top of Mount Snow for Typhoon Nari [see $x = -100$ to -80 km in Fig. 8c of Yang et al. (2011a)]. This implies that as convective cells propagate upslope, raindrops fall out rapidly and seldom evaporate in the near-saturated environment, and the increase of liquid-phase condensation produces rapid increase of precipitation efficiency. As cell A moves to the CMR lee side, the PE and CR are reduced to less than 50% and less than 80%, respectively (Fig. 12a). For cell B moving across a steeper terrain than cell A (Fig. 10), the range of changes in PE and CR in the upslope and downslope processes are larger than those for cell A, indicating different microphysics responses even for a slight variation of terrain height and slope under the same southwestern CMR. The Lagrangian evolution of PE and three microphysics ratios for cells C and D as shown in Fig. 14 are basically similar to those for cells A and B as shown in Fig. 12, except for a smaller range of changes of DR and ER on a gentler lee side.

To further verify the Lagrangian evolution of PE and three microphysics ratios for four major convective cells, Fig. 15 illustrates the changes of the same four microphysical parameters across the mountain, but from an Eulerian framework, for two time- and space-averaged cross sections across the southern CMR (see Figs. 10b and 11c for the corresponding locations) at times of convective cells along the west–east rainbands constantly impinging on the steep southern Taiwan terrain. The microphysics parameters in two cross sections all show an increase of PE on the windward side and a decrease on the lee side; on the other hand, the DR and ER are decreased on the windward side but substantially increased on the lee side. The increase of DR and some minor increase of PE on the lee side result from decrease of liquid-phase condensation as the air on the lee side subsides and moves downstream.

4. Conclusions

In this study, the Advanced Research Weather Research and Forecasting model (ARW), version 3.2 was used with triply nested grids with a finest grid size of 1 km (without using any cumulus parameterization on three nested domains) to explicitly simulate the track, rainfall distribution, and the convective cells along the outer rainbands of Typhoon Morakot (2009), which dumped rainfall of more than 2600 mm in 3 days on Taiwan. In addition to a full-terrain control run (CTL), a no-terrain sensitivity experiment (FLAT) was conducted to investigate the orographic effects of the Taiwan Central Mountain Range (CMR) on vapor and water budgets and precipitation efficiency of Morakot during landfall.

The control simulation captures reasonably well the track, precipitation structure, and outer rainbands of Morakot as verified against the best-track, radar, and rain gauge observations. Some model deficiencies still exist; for example, the landfall location is 17 km north of the observed location with a landfall time 8–10 h later (for a 42-h forecast), and the local rainfall maximum is slightly overestimated over the central CMR and slightly underestimated over southern Taiwan. During the landfall period, the CTL captured the slow movement of vortex circulation, the quasi-stationary “T” shape rainfall maxima at the intersection between outer rainband and the CMR, and some local rainfall maxima in southwestern Taiwan. The high-resolution model output (with 1-km grid size and 2-min data interval) is used to calculate the water vapor and condensate (clouds and precipitation) budgets and precipitation efficiency. Results show that the calculated precipitation efficiency is highly correlated with the surface rain rate;

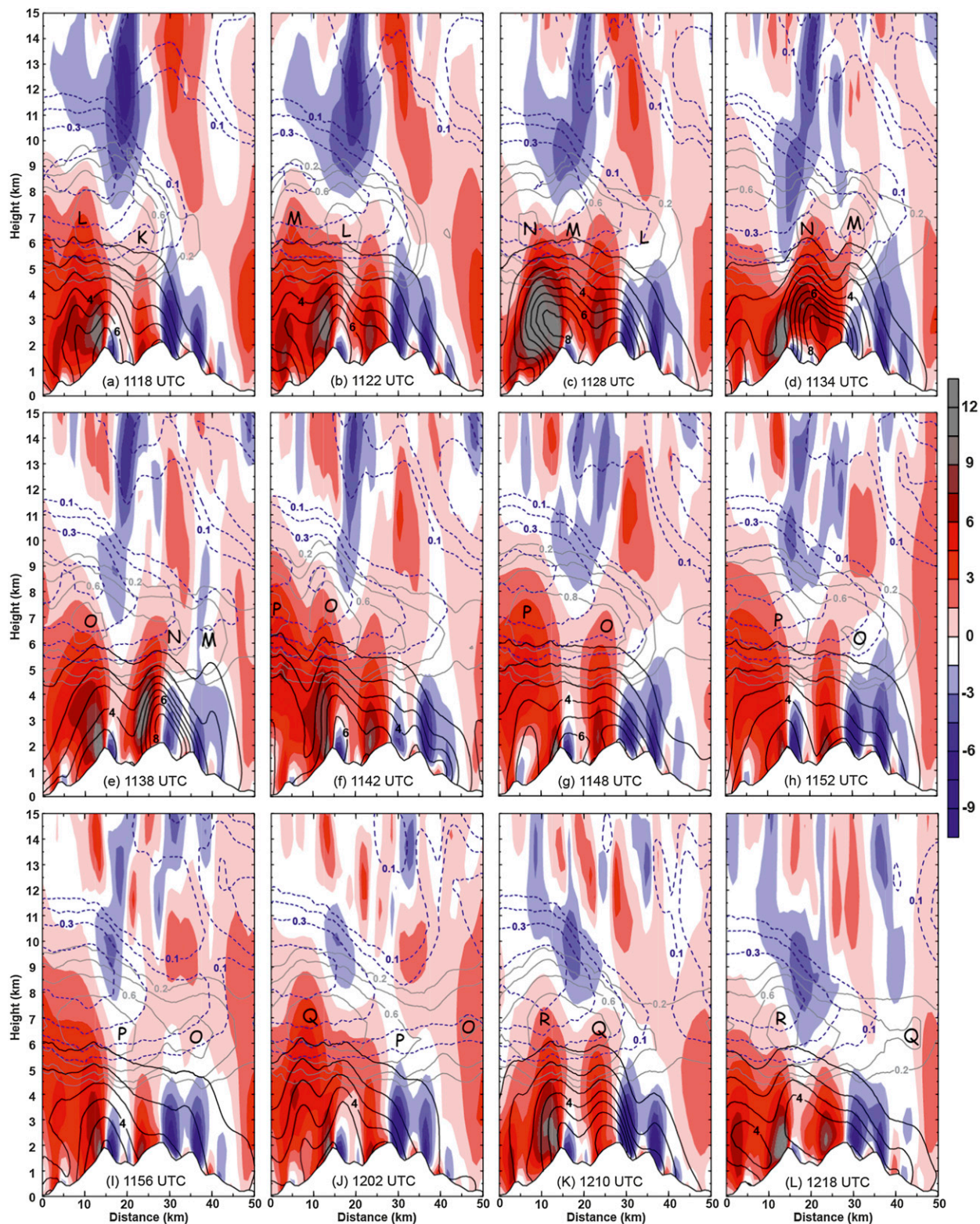


FIG. 13. Vertical cross section along the white line in Fig. 4b of mixing ratios of snow (blue dashed; 0.1 g kg^{-1} interval), graupel (gray; 0.2 g kg^{-1} interval), and rainwater (black; 1 g kg^{-1} interval), superimposed with vertical velocity (shaded by the color bar) of the CTL run. Convective cells K, L, M, N, O, P, Q, and R are indicated. The time (UTC) is at the bottom of each panel.

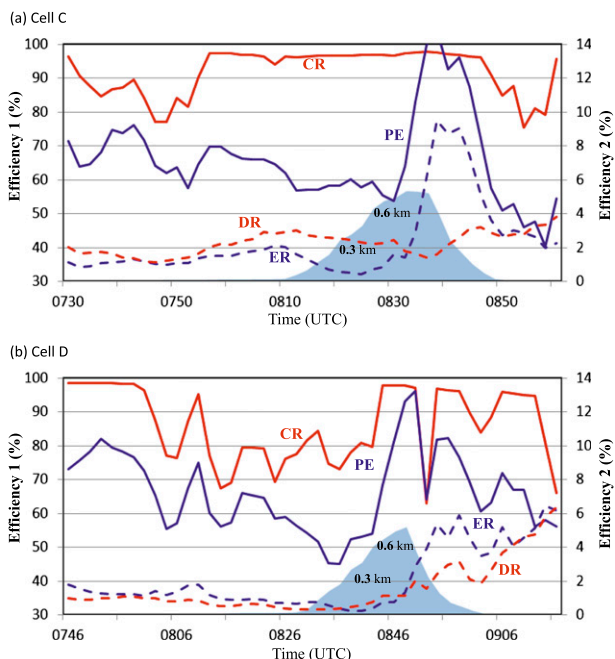


FIG. 14. As in Fig. 12, but for (a) cell C and (b) cell D calculated within the black boxes on the 1-km grid in Fig. 11. The light blue shading is terrain height passed by cells C and D. The PE (blue solid) and CR (red solid) correspond to efficiency 1 (left ordinate), and DR (red dashed) and ER (blue dashed) correspond to efficiency 2 (right ordinate).

in particular, the precipitation efficiency can reach more than 95% when the surface rate is greater than 50 mm h^{-1} over the CMR. For the whole vortex circulation, the 1-h-averaged PE of Morakot is about 66%, similar to that of Nari (2001). Despite their different track and storm structure, a common water-budget feature between Morakot and Nari is that both have enhanced water vapor convergence, increased PE, and greater surface precipitation after landfall on Taiwan. For a local box area ($49.5 \text{ km} \times 106.5 \text{ km}$) with heavy rainfall in southwestern CMR, the PE of Morakot remains 75%–100% for 6 h, producing torrential rainfalls and severe land- and mudslides that eventually buried the entire village of Shiaolin and killed approximately 500 people in the village (Wu and Yang 2011).

The no-terrain sensitivity experiment is used to compare with the full-terrain control simulation to highlight the interaction between Morakot circulation and Taiwan terrain. In the absence of Taiwan topography, the FLAT storm turns northward earlier than the CTL storm, probably because of enhanced westward pressure gradient acceleration by the strong latent heating associated with heavy orographic rainfall in the CTL run [see Fig. 20 of Yang and Ching (2005) and Figs. 6 and 7 of Hsu et al. (2013)]. The rainfall pattern is mainly

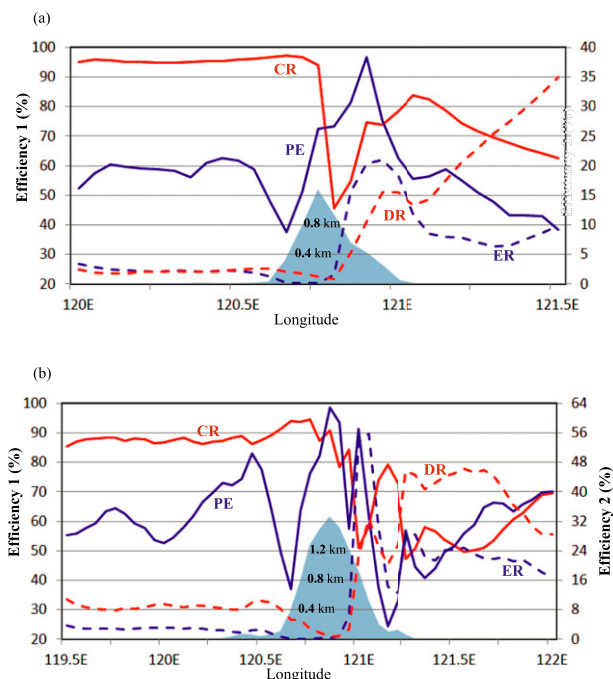


FIG. 15. Horizontal cross section of PE, CR, DR, and ER averaged in the latitudinal direction of 36 km for the dashed box in (a) Fig. 11c and (b) Fig. 10b. Cross section in (a) is also temporally averaged for 90 min (1100–1230 UTC) and cross section in (b) is averaged for 70 min (0800–0910 UTC 8 Aug 2009). The PE (blue solid) and CR (red solid) correspond to efficiency 1 (left ordinate), and DR (red dashed) and ER (blue dashed) correspond to efficiency 2 (right ordinate).

dominated by Morakot outer rainbands in the FLAT run. The simulated rain rate and PE of the FLAT storm are 50% and 15%–20% less than those of the CTL storm over Taiwan during Morakot’s landfall period.

A semi-Lagrangian framework is adopted to investigate the “in situ” orographic forcing of the CMR on the microphysical processes by following the eastward propagation of four major convective cells along the quasi-stationary west–east rainbands (starting from the Taiwan Strait, above the southern CMR, and to the lee side of CMR). The Lagrangian evolution is also confirmed by the changes of microphysical processes across the CMR along a time- and space-averaged cross section in the Eulerian framework. The PEs are 45%–80% for oceanic rainfall regime and more than 95% for mountain rainfall regime, respectively. The extremely high PE ($>95\%$) at the mountain rainfall regime mainly results from the increase of cloud condensation and the decrease of raindrop evaporation through the CMR orographic lifting. On the other hand, the low PE ($<50\%$) on the lee side is caused by the strong increase of raindrop evaporation and the decrease of cloud condensation. The secondary increase of the PEs results from the

increase of ice-phase deposition ratio when the liquid-phase condensation becomes small as the air on the lee side subsides and propagates downstream.

Slow movement of Typhoon Morakot, persistent transport of abundant moisture by the southwesterly monsoon flow from the ocean, and the local rainfall enhancement by the steep Taiwan topography all contribute to the almost world record of extreme typhoon rainfall on Taiwan (>2600 mm in 3 days). Finally, the conclusions obtained in this study are mainly based on numerical simulations with some model deficiencies, physics uncertainties, and numerical errors; thus, we should keep these caveats in mind. Further analyses are required to generalize the findings from this particular typhoon case to other tropical cyclones in other geographical locations (such as the Atlantic Ocean or Australia) and also to other precipitation regimes (midlatitude frontal system and tropical cloud clusters).

Acknowledgments. We appreciate three anonymous reviewers' helpful comments, which significantly improved the quality of this manuscript. This work was supported by the National Science Council of Taiwan under Grants NSC 98-2811-M-008-026, NSC 100-2745-M-002-003-ASP, NSC 101-2745-M-002-003-ASP, and NSC 101-2119-M-008-015.

REFERENCES

- Auer, A. H., Jr., and J. D. Marwitz, 1968: Estimates of air and moisture flux into hailstorms on the High Plains. *J. Appl. Meteor.*, **7**, 196–198.
- Braham, R. R., Jr., 1952: The water and energy budgets of the thunderstorm and their relation to thunderstorm development. *J. Meteor.*, **9**, 227–242.
- Braun, S. A., 2006: High-resolution simulation of Hurricane Bonnie (1998). Part II: Water budget. *J. Atmos. Sci.*, **63**, 43–64.
- Chien, F.-C., and H.-C. Kuo, 2011: On the extreme rainfall of Typhoon Morakot (2009). *J. Geophys. Res.*, **116**, D05104, doi:10.1029/2010JD015092.
- Doswell, C. A., III, H. E. Brooks, and R. A. Maddox, 1996: Flash flood forecasting: An ingredients-based methodology. *Wea. Forecasting*, **11**, 560–581.
- Dudhia, J., 1989: Numerical simulation of convection observed during the Winter Monsoon Experiment using a mesoscale two-dimensional model. *J. Atmos. Sci.*, **46**, 3077–3107.
- Fang, X., Y.-H. Kuo, and A. Wang, 2011: The impacts of Taiwan topography on the predictability of Typhoon Morakot's record-breaking rainfall: A high-resolution ensemble simulation. *Wea. Forecasting*, **26**, 613–633.
- Ferrier, B. S., J. Simpson, and W.-K. Tao, 1996: Factors responsible for precipitation efficiencies in midlatitude and tropical squall simulations. *Mon. Wea. Rev.*, **124**, 2100–2125.
- Ge, X., T. Li, S. Zhang, and M. Peng, 2010: What causes the extremely heavy rainfall in Taiwan during Typhoon Morakot (2009)? *Atmos. Sci. Lett.*, **11**, 46–50, doi:10.1002/asl.255.
- Heymsfield, G. M., and S. Schotz, 1985: Structure and evolution of a severe squall line over Oklahoma. *Mon. Wea. Rev.*, **113**, 1563–1589.
- Hong, C.-C., M.-Y. Lee, H.-H. Hsu, and J.-L. Kuo, 2010: Role of submonthly disturbance and 40–50 day ISO on the extreme rainfall event associated with typhoon Morakot (2009) in Southern Taiwan. *Geophys. Res. Lett.*, **37**, L08805, doi:10.1029/2010GL042761.
- Hong, S.-Y., and H.-L. Pan, 1996: Nonlocal boundary layer vertical diffusion in a medium-range forecast model. *Mon. Wea. Rev.*, **124**, 2322–2339.
- , and J.-O. J. Lim, 2006: The WRF single-moment microphysics scheme (WSM6). *J. Korean Meteor. Soc.*, **42**, 129–151.
- , Y. Noh, and J. Dudhia, 2006: A new vertical diffusion package with an explicit treatment of entrainment processes. *Mon. Wea. Rev.*, **134**, 2318–2341.
- Hsu, L.-H., H.-C. Kuo, and R. G. Fovell, 2013: On the geographic asymmetry of typhoon translation speed across the mountainous island of Taiwan. *J. Atmos. Sci.*, **70**, 1006–1022.
- Huang, C.-Y., C.-S. Wong, and T.-C. Yeh, 2011: Extreme rainfall mechanisms exhibited by Typhoon Morakot. *Terr. Atmos. Ocean. Sci.*, **22**, 613–632.
- Jian, G.-J., and C.-C. Wu, 2008: A numerical study of the track deflection of Supertyphoon Haitang (2005) prior to its landfall in Taiwan. *Mon. Wea. Rev.*, **136**, 598–615.
- Kurihara, Y., 1975: Budget analyses of a tropical cyclone simulated in an axisymmetric numerical model. *J. Atmos. Sci.*, **32**, 25–59.
- Lee, C.-S., Y.-C. Liu, and F.-C. Chien, 2008: The secondary low and heavy rainfall associated with Typhoon Mindule (2004). *Mon. Wea. Rev.*, **136**, 1260–1283.
- Li, X., C.-H. Sui, and K.-M. Lau, 2002a: Precipitation efficiency in the tropical deep convective regime: A 2-D cloud resolving modeling study. *J. Meteor. Soc. Japan*, **80**, 205–212.
- , —, and —, 2002b: Dominant cloud microphysical processes in a tropical oceanic convective system: A 2D cloud resolving modeling study. *Mon. Wea. Rev.*, **130**, 2481–2491.
- Lin, C.-Y., H.-M. Hsu, Y.-F. Sheng, C.-H. Kuo, and Y.-A. Liou, 2011: Mesoscale processes for super heavy rainfall of Typhoon Morakot (2009) over Southern Taiwan. *Atmos. Chem. Phys.*, **11**, 345–361.
- Lin, Y.-L., S.-Y. Chen, C. M. Hill, and C.-Y. Huang, 2005: Control parameters for the influence of a mesoscale mountain range on cyclone track continuity and deflection. *J. Atmos. Sci.*, **62**, 1849–1866.
- Malkus, J., and H. Riehl, 1960: On the dynamics and energy transformations in steady-state hurricanes. *Tellus*, **12**, 1–20.
- Marks, F. D., Jr., and R. A. Houze Jr., 1987: Inner core structure of Hurricane Alicia from airborne Doppler radar observations. *J. Atmos. Sci.*, **44**, 1296–1317.
- Mlawer, E. J., S. J. Taubman, P. D. Brown, M. J. Iacono, and S. A. Clough, 1997: Radiative transfer for inhomogeneous atmospheres: RRTM, a validated correlated-k model for the longwave. *J. Geophys. Res.*, **102** (D14), 16 663–16 682.
- Skamarock, W. C., and Coauthors, 2008: A description of the Advanced Research WRF version 3. NCAR Tech. Note NCAR/TN-475+STR, 113 pp. [Available online at http://www.mmm.ucar.edu/wrf/users/docs/arw_v3_bw.pdf.]
- Sui, C.-H., X. Li, M.-J. Yang, and H.-L. Huang, 2005: Estimation of oceanic precipitation efficiency in cloud models. *J. Atmos. Sci.*, **62**, 4358–4370.
- , —, and —, 2007: On the definition of precipitation efficiency. *J. Atmos. Sci.*, **64**, 4506–4513.

- Tang, X.-D., M.-J. Yang, and Z.-M. Tan, 2012: A modeling study of orographic convection and mountain waves in the land-falling typhoon Nari (2001). *Quart. J. Roy. Meteor. Soc.*, **138**, 419–438.
- Tao, W.-K., and Coauthors, 2011: High-resolution numerical simulation of Typhoon Morakot. Part I: The impact of microphysics and PBL. *Terr. Atmos. Ocean. Sci.*, **22**, 673–696.
- Wu, C.-C., and Y.-H. Kuo, 1999: Typhoons affecting Taiwan: Current understanding and future challenges. *Bull. Amer. Meteor. Soc.*, **80**, 67–80.
- , and M.-J. Yang, 2011: Preface to the special issue on “Typhoon Morakot (2009): Observation, modeling, and forecasting.” *Terr. Atmos. Ocean. Sci.*, **22**, doi:10.3319/TAO.2011.10.01.01(TM).
- , T.-H. Yen, Y.-H. Kuo, and W. Wang, 2002: Rainfall simulation associated with Typhoon Herb (1996) near Taiwan. Part I: The topographic effect. *Wea. Forecasting*, **17**, 1001–1015.
- Yang, M.-J., and L. Ching, 2005: A modeling study of Typhoon Toraji (2001): Physical parameterization sensitivity and topographic effect. *Terr. Atmos. Ocean. Sci.*, **16**, 177–213.
- , D.-L. Zhang, and H.-L. Huang, 2008: A modeling study of Typhoon Nari (2001) at landfall. Part I: Topographic effects. *J. Atmos. Sci.*, **65**, 3095–3115.
- , S. A. Braun, and D.-S. Chen, 2011a: Water budget of Typhoon Nari (2001) at landfall. *Mon. Wea. Rev.*, **139**, 3809–3828.
- , D.-L. Zhang, X.-D. Tang, and Y. Zhang, 2011b: A modeling study of Typhoon Nari (2001) at landfall. Part II: Structural changes and terrain-induced asymmetries. *J. Geophys. Res.*, **116**, D09112, doi:10.1029/2010JD015445.
- Yeh, T.-C., and R. L. Elsberry, 1993a: Interaction of typhoons with the Taiwan orography. Part I: Upstream track deflections. *Mon. Wea. Rev.*, **121**, 3193–3213.
- , and —, 1993b: Interaction of typhoons with the Taiwan orography. Part II: Continuous and discontinuous tracks across the island. *Mon. Wea. Rev.*, **121**, 3213–3233.